

Origin of meteoritic stardust unveiled by a new proton-capture rate of oxygen-17

M. Lugaro^{1,2,*}, A. I. Karakas^{2,3,4}, C. G. Bruno⁵, M. Aliotta⁵, L. R. Nittler⁶, D. Bemmerer⁷, A. Best⁸, A. Boeltzig⁹, C. Broggini¹⁰, A. Caciolli¹¹, F. Cavanna¹², G. F. Ciani⁹, P. Corvisiero¹², T. Davinson⁵, R. Depalo¹¹, A. Di Leva⁸, Z. Elekes¹³, F. Ferraro¹², A. Formicola¹⁴, Zs. Fülöp¹³, G. Gervino¹⁵, A. Guglielmetti¹⁶, C. Gustavino¹⁷, Gy. Gyürky¹³, G. Imbriani⁸, M. Junker¹⁴, R. Menegazzo¹⁰, V. Mossa¹⁸, F. R. Pantaleo¹⁸, D. Piatti¹¹, P. Prati¹², D. A. Scott⁵, O. Straniero¹⁹, F. Strieder^{20,21}, T. Szücs¹³, M. P. Takács⁷, D. Trezzi¹⁶

**Corresponding author*

¹*Konkoly Observatory, Research Centre for Astronomy and Earth Sciences, Hungarian Academy of Sciences, H-1121 Budapest, Hungary*

²*Monash Centre for Astrophysics (MoCA), Monash University, Clayton VIC 3800, Australia*

³*Research School of Astronomy and Astrophysics, Australian National University, Canberra, ACT 2611, Australia*

⁴*Kavli Institute for the Physics and Mathematics of the Universe (WPI), University of Tokyo, Kashiwa, Chiba 277-8583, Japan*

⁵*SUPA, School of Physics and Astronomy, University of Edinburgh, EH9 3FD Edinburgh, United Kingdom*

⁶*Department of Terrestrial Magnetism, Carnegie Institution for Science, Washington, DC 20015, USA*

⁷*Helmholtz-Zentrum Dresden-Rossendorf, Bautzner Landstr. 400, 01328 Dresden, Germany*

⁸*Università di Napoli Federico II and INFN, Sezione di Napoli, 80126 Napoli, Italy*

⁹*Gran Sasso Science Institute, INFN, Viale F. Crispi 7, 67100 L'Aquila, Italy*

¹⁰*INFN of Padova, Via Marzolo 8, I-35131 Padova, Italy*

¹¹*Università degli Studi di Padova and INFN, Sezione di Padova, Via F. Marzolo 8, 35131 Padova, Italy*

¹²*Università degli Studi di Genova and INFN, Sezione di Genova, Via Dodecaneso 33, 16146 Genova, Italy*

¹³*Institute for Nuclear Research (MTA ATOMKI), PO Box 51, HU-4001 Debrecen, Hungary*

¹⁴*INFN, Laboratori Nazionali del Gran Sasso (LNGS), 67100 Assergi, Italy*

¹⁵*Università degli Studi di Torino and INFN, Sezione di Torino, Via P. Giuria 1, 10125 Torino, Italy*

¹⁶*Università degli Studi di Milano and INFN, Sezione di Milano, Via G. Celoria 16, 20133 Milano, Italy*

¹⁷*INFN, Sezione di Roma La Sapienza, Piazzale A. Moro 2, 00185 Roma, Italy*

¹⁸*Università degli Studi di Bari and INFN, Sezione di Bari, 70125 Bari, Italy*

¹⁹*Osservatorio Astronomico di Collurania, Teramo, and INFN, Sezione di Napoli, 80126 Napoli, Italy*

²⁰*Institut für Experimentalphysik III, Ruhr-Universität Bochum, 44780 Bochum, Germany*

²¹*Present address: South Dakota School of Mines, 501 E. Saint Joseph St., SD 57701 USA*

Stardust grains recovered from meteorites provide high-precision snapshots of the isotopic

composition of the stellar environment in which they formed¹. Attributing their origin to specific types of stars, however, often proves difficult. Intermediate-mass stars of 4-8 solar masses are expected to contribute a large fraction of meteoritic stardust^{2,3}. However, no grains have been found with characteristic isotopic compositions expected from such stars^{4,5}. This is a long-standing puzzle, which points to serious gaps in our understanding of the lifecycle of stars and dust in our Galaxy. Here we show that the increased proton-capture rate of ^{17}O reported by a recent underground experiment⁶ leads to $^{17}\text{O}/^{16}\text{O}$ isotopic ratios that match those observed in a population of stardust grains, for proton-burning temperatures of 60–80 million K. These temperatures are indeed achieved at the base of the convective envelope during the late evolution of intermediate-mass stars of 4-8 solar masses^{7–9}, which reveals them as the most likely site of origin of the grains. This result provides the first direct evidence that these stars contributed to the dust inventory from which the Solar System formed.

Stardust grains found in meteorites (and also interplanetary dust particles and samples returned from comet Wild 2) represent the very small fraction of presolar dust that survived destruction in the protosolar nebula. They condensed in the atmospheres of evolved stars and in nova and supernova ejecta and were preserved inside meteorites¹. Their isotopic compositions are measured with high precision (few percent uncertainties) via mass spectrometry and represent a direct record of their site of formation, providing us with deep insights into stellar physics and the origin of elements and of dust in the Galaxy. Identified stardust includes both carbon-rich (diamonds, graphite, silicon carbide) and oxygen-rich (e.g., Al-rich oxides, silicate) grains, with the former condensing

from gas with $C > O$, and the latter from gas with $C < O$. Here we focus on oxide and silicate grains, which are classified into different groups mostly based on their oxygen isotopic compositions¹⁰. Group I grains make up the majority ($\sim 75\%$) of oxide and silicate grains and show excesses in ^{17}O characteristic of the first dredge-up in red giant stars of initial mass roughly $1\text{--}3\text{ }M_{\odot}$, with a maximum $^{17}\text{O}/^{16}\text{O} \sim 0.003$. Their origin is generally well understood and attributed to the O-rich phases of the subsequent asymptotic giant branch (AGB), when large amounts of dust condense in the cool, expanding stellar envelopes². Group II grains represent roughly 10% of all presolar oxide grains, although this is a lower limit since measured compositions may suffer from isotopic dilution during ion probe analysis. Like Group I grains they display excesses in ^{17}O (with $^{17}\text{O}/^{16}\text{O}$ up to 0.0015), but are also highly depleted in ^{18}O , with $^{18}\text{O}/^{16}\text{O}$ ratios down by two orders of magnitude relative to the solar value. The initial ratio of the radioactive ^{26}Al (half life, $T_{1/2} = 0.7\text{ Myr}$) to ^{27}Al is inferred from ^{26}Mg excesses and in Group II grains reaches 0.1, almost an order of magnitude higher than in Group I grains, on average. While this composition is the indisputable signature of H burning activating proton captures on the oxygen isotopes and on ^{25}Mg (the $^{25}\text{Mg}(p,\gamma)^{26}\text{Al}$ reaction), hypotheses on the site of formation of Group II grains are still tentative.

Hydrogen burning affects the surface composition of massive ($> 4\text{ }M_{\odot}$) AGB stars when the base of the convective envelope becomes hot enough for proton-capture nucleosynthesis to occur⁷ (“hot bottom burning”, HBB, Figure 1). These are the brightest AGB stars, and the fact that they mostly show $C/O < 1$ is attributed to the operation of the CN cycle, which depletes carbon¹¹, in contrast to their less bright counterparts, which mostly show $C/O > 1$ as a result of the dredge-up of He-burning material rich in carbon. Characteristic temperatures of HBB exceed $\sim 60\text{ MK}$ and,

thanks to the fast convective turn-over time (≈ 1 yr), the composition of the whole envelope is quickly transmuted into the H-burning equilibrium abundances produced at the base of the envelope. Massive AGB stars are observed to generate significant amounts of dust and based on current models of Galactic dust evolution are expected to have contributed almost half of the O-rich dust of AGB origin in the Solar System^{2,3}. However, no stardust grains have been found to show the signature of HBB because, although Group II grains show the highly depleted $^{18}\text{O}/^{16}\text{O}$ ratios qualitatively expected from HBB, their $^{17}\text{O}/^{16}\text{O}$ ratios are roughly two-times lower than predicted^{4,5} using the available reaction rates¹².

Currently, the preferred suggestion for the origin of Group II grains is that they formed in AGB stars of low mass ($<1.5 M_{\odot}$) that did not dredge-up enough carbon to become C-rich but experienced extra mixing below the bottom of the convective envelope (“cool bottom processing”, CBP^{13,14}, Figure 1). In this scenario, material from the bottom of the convective envelope penetrates the thin radiative region located between the base of the convective envelope and the top of the H-burning shell where the temperature and density increase steeply with mass depth and proton captures can occur (Figure 1). While mechanisms have been proposed to explain the physical process driving this extra mixing¹⁵ the current modelling of the CBP is parametric: both the rate of the extra mixing and the depth reached are treated as free parameters, with the depth adjusted in order to reach temperatures in the range 40–55 MK.

Whichever scenario we consider, the equilibrium $^{17}\text{O}/^{16}\text{O}$ ratio produced by H burning is determined by the competition between the processes that produce and destroy ^{17}O . Specifically, it

depends on the ratio between the rate of the $^{16}\text{O}(\text{p},\gamma)^{17}\text{F}$ reaction, which produces ^{17}O following the beta decay of ^{17}F ($T_{1/2} = 64$ s), and the rate of the $^{17}\text{O}(\text{p},\alpha)^{14}\text{N}$ reaction, which destroys ^{17}O . (Note that the $^{17}\text{O}(\text{p},\gamma)^{18}\text{F}$ is comparatively negligible at all temperatures considered here). The former is known to within 7%^{5,12}; the latter has recently been determined⁶ from a direct measurement of the strength of the 64.5 keV resonance that dominates the $^{17}\text{O}(\text{p},\alpha)^{14}\text{N}$ reaction rate at temperatures between 10 and 100 MK⁶, i.e., over the entire range of interest here. The experiment took place at the Laboratory for Underground Nuclear Astrophysics (LUNA) at Gran Sasso, Italy, where improved experimental procedures and a 15-times lower background for α particles detection than in surface laboratories allowed for the most sensitive measurement to date⁶. The new rate is 2–2.5 times higher than previous evaluations^{12,16}. At the temperatures of 40–55 MK typical of CBP the new rate reproduces only the lowest $^{17}\text{O}/^{16}\text{O}$ values observed in Group II grains (Figure 2). At the temperatures of 60–80 MK typical of HBB, instead, the new rate reproduces most of the observed $^{17}\text{O}/^{16}\text{O}$ range, revealing for the first time the signature expected from HBB in stardust grains. HBB temperatures higher than ~ 80 MK are excluded for the parent stars of the grains.

Although the initial stellar mass and metallicity ranges at which HBB occurs as well as the AGB lifetime are model dependent^{7–9}, our result is robust because any massive AGB model experiencing HBB with temperatures between 60 and 80 MK will necessarily produce $^{17}\text{O}/^{16}\text{O}$ ratios in agreement with those observed in most Group II grains. Figure 3 shows the surface evolution of the oxygen isotopic ratios for three AGB models (of initial mass 4.5, 5, and 6 M_{\odot}) of solar metallicity that experience HBB (see Methods section), compared to observed isotopic ratios in Group II stardust grains. The models evolve through the first and second dredge-ups at

the end of core H- and He-burning, respectively, which increase the $^{17}\text{O}/^{16}\text{O}$ ratio by roughly a factor of five. During the subsequent AGB phase, HBB quickly (e.g., after about 1/5 of its total TP-AGB lifetime for a $6M_{\odot}$ star) shifts the oxygen isotopic composition to the equilibrium values corresponding to the burning temperature. Using the LUNA rate, the $^{17}\text{O}/^{16}\text{O}$ ratio produced by HBB is roughly a factor of 2 lower than that obtained with the previous rate by Iliadis *et al.*¹² and nicely reproduces those observed in Group II grains, when AGB material is diluted with material of solar composition. The dilution is required because HBB strongly depletes ^{18}O . This is in accordance with the non-detection of ^{18}O in bright O-rich AGB stars¹⁷, but results in $^{18}\text{O}/^{16}\text{O}$ ratios more than two orders of magnitude lower than observed in Group II grains. Dilution with solar material is particularly effective in increasing the $^{18}\text{O}/^{16}\text{O}$ ratio: for example, 99% of HBB material mixed with only 1% of solar material increases the $^{18}\text{O}/^{16}\text{O}$ by two orders of magnitudes. On the other hand, dilution has a comparatively minor effect on the other isotopes measured in the grains because ^{17}O , ^{25}Mg , and ^{26}Al are *produced* rather than *destroyed* in massive AGB stars. For example, it takes dilution with 50% of solar system material to decrease the $^{17}\text{O}/^{16}\text{O}$ and $^{25}\text{Mg}/^{24}\text{Mg}$ ratios by a factor of 2.

Dilution can be wrought by percent-level traces of contaminant oxygen (e.g., from terrestrial or non-presolar material) during isotopic measurements, which can result in $^{18}\text{O}/^{16}\text{O}$ up to $\sim 10^{-4}$; however, laboratory contamination cannot easily explain grains with higher $^{18}\text{O}/^{16}\text{O}$ values. For these, a dilution of the HBB signature composition with solar system material at the level of a few tens of percent is required. Even higher dilution would result in a fraction of Group I grains also originating from massive AGB stars. Possible processes may involve dilution with previously

ejected gas within the dust formation region; dilution with material in the interstellar medium; and/or a significantly lower value of the $^{18}\text{O}(\text{p},\alpha)^{15}\text{N}$ reaction rate. A study of this reaction has recently been completed at LUNA and data analysis is in progress.

The other isotopic pairs measured in Group II grains are also consistent with an origin in massive AGB stars. The $^{25}\text{Mg}/^{24}\text{Mg}$ ratios are enhanced in massive AGB stars by the third dredge-up of material from the He inter-shell, where the $^{22}\text{Ne}(\alpha,\text{n})^{25}\text{Mg}$ reaction is activated, and such a signature is seen in some presolar spinel (MgAl_2O_4) grains (Figure 4a). Specifically, the two times solar $^{25}\text{Mg}/^{24}\text{Mg}$ value observed in a spinel grain named 14-12-7¹⁸ is close to that obtained in the final composition of the 5 M_\odot model. However, grain OC2⁴ and the majority of the other grains show a spread in the $^{25}\text{Mg}/^{24}\text{Mg}$ ratio from 1 to 1.5 times solar, i.e., lower than predicted by the dilution computed using the final AGB composition. This may reflect partial equilibration of Mg isotopes in the grains themselves¹⁹. Alternatively, the lower $^{25}\text{Mg}/^{24}\text{Mg}$ ratios may be explained by truncating the AGB evolution to one-half or one-third of the total computed evolution (as illustrated in Figures 3 and 4). This could result from a higher mass-loss rate and/or the effect of binary interactions. Another solution allowed within current model uncertainties is a less efficient third dredge-up than calculated in our models. Finally, the high $^{26}\text{Al}/^{27}\text{Al}$ ratios up to ~ 0.1 typical of Group II grains are also consistent with HBB (Figure 4b), although an accurate analysis is currently hampered by the uncertainties in the ^{25}Mg and ^{26}Al proton-capture rates^{12,20}.

Our evidence that some meteoritic stardust grains exist whose O, Mg, and Al isotopic composition is best accounted for by H-burning conditions characteristic of massive AGB stars proves

that these stars were dust contributors to the early Solar System. It further provides us with a new tool to deepen our understanding of uncertain physical processes in massive AGB stars, for which observational constraints are still scarce.

1. Zinner, E. Presolar Grains. In Davis, A. M. (ed.) *Microphysics of Cosmic Plasmas*, 181–213 (2014).
2. Gail, H.-P., Zhukovska, S. V., Hoppe, P. & Tieloff, M. Stardust from Asymptotic Giant Branch Stars. *Astrophys. J.* **698**, 1136–1154 (2009).
3. Zhukovska, S., Petrov, M. & Henning, T. Can Star Cluster Environment Affect Dust Input From Massive AGB Stars? *Astrophys. J.* **810**, 128 (2015).
4. Lugaro, M. *et al.* On the asymptotic giant branch star origin of peculiar spinel grain OC2. *Astron. Astrophys.* **461**, 657–664 (2007).
5. Iliadis, C., Angulo, C., Descouvemont, P., Lugaro, M. & Mohr, P. New reaction rate for $^{16}\text{O}(p,\gamma)^{17}\text{F}$ and its influence on the oxygen isotopic ratios in massive AGB stars. *Phys. Rev. C* **77**, 045802 (2008).
6. Bruno, C. G. *et al.* Improved direct measurement of the 64.5 keV resonance strength in the $^{17}\text{O}(p,\alpha)^{14}\text{N}$ reaction at LUNA. *Phys. Rev. Lett.* accepted (2016).
7. Ventura, P., Di Criscienzo, M., Carini, R. & D’Antona, F. Yields of AGB and SAGB models with chemistry of low- and high-metallicity globular clusters. *Mon. Not. R. Astron. Soc.* **431**, 3642–3653 (2013).

8. Cristallo, S., Straniero, O., Piersanti, L. & Gobrecht, D. Evolution, Nucleosynthesis, and Yields of AGB Stars at Different Metallicities. III. Intermediate-mass Models, Revised Low-mass Models, and the ph-FRUITY Interface. *Astrophys. J. Suppl.* **219**, 40 (2015).
9. Karakas, A. I. & Lugaro, M. Stellar yields from metal-rich asymptotic giant branch models. *Astrophys. J.* (2016).
10. Nittler, L. R., Alexander, C. M. O., Gao, X., Walker, R. M. & Zinner, E. Stellar Sapphires: The Properties and Origins of Presolar AL 2O 3 in Meteorites. *Astrophys. J.* **483**, 475 (1997).
11. Wood, P. R., Bessell, M. S. & Fox, M. W. Long-period variables in the Magellanic Clouds - Supergiants, AGB stars, supernova precursors, planetary nebula precursors, and enrichment of the interstellar medium. *Astrophys. J.* **272**, 99–115 (1983).
12. Iliadis, C., Longland, R., Champagne, A. E., Coc, A. & Fitzgerald, R. Charged-particle thermonuclear reaction rates: II. Tables and graphs of reaction rates and probability density functions. *Nuclear Physics A* **841**, 31–250 (2010).
13. Nollett, K. M., Busso, M. & Wasserburg, G. J. Cool Bottom Processes on the Thermally Pulsing Asymptotic Giant Branch and the Isotopic Composition of Circumstellar Dust Grains. *Astrophys. J.* **582**, 1036–1058 (2003).
14. Palmerini, S., La Cognata, M., Cristallo, S. & Busso, M. Deep Mixing in Evolved Stars. I. The Effect of Reaction Rate Revisions from C to Al. *Astrophys. J.* **729**, 3 (2011).

15. Nucci, M. C. & Busso, M. Magnetohydrodynamics and Deep Mixing in Evolved Stars. I. Two- and Three-dimensional Analytical Models for the Asymptotic Giant Branch. *Astrophys. J.* **787**, 141 (2014).
16. Buckner, M. Q. *et al.* High-intensity-beam study of $^{17}\text{O}(p, \gamma)^{18}\text{F}$ and thermonuclear reaction rates for $^{17}\text{O}+p$. *Phys. Rev. C* **91**, 015812 (2015).
17. Justtanont, K. *et al.* Herschel observations of extreme OH/IR stars. The isotopic ratios of oxygen as a sign-post for the stellar mass. *Astron. Astrophys.* **578**, A115 (2015).
18. Gyngard, F. *et al.* Automated NanoSIMS Measurements of Spinel Stardust from the Murray Meteorite. *Astrophys. J.* **717**, 107–120 (2010).
19. Nittler, L. R. *et al.* Aluminum-, Calcium- and Titanium-rich Oxide Stardust in Ordinary Chondrite Meteorites. *Astrophys. J.* **682**, 1450–1478 (2008).
20. Straniero, O. *et al.* Impact of a Revised $^{25}\text{Mg}(p, \gamma)^{26}\text{Al}$ Reaction Rate on the Operation of the Mg-Al Cycle. *Astrophys. J.* **763**, 100 (2013).
21. Hynes, K. M. & Gyngard, F. The Presolar Grain Database: <http://presolar.wustl.edu/~pgd>. In *Lunar and Planetary Science Conference*, vol. 40 of *Lunar and Planetary Science Conference*, 1198 (2009).
22. Asplund, M., Grevesse, N., Sauval, A. J. & Scott, P. The Chemical Composition of the Sun. *Ann. Rev. Astron. Astrophys.* **47**, 481–522 (2009).

23. Karakas, A. I. Helium enrichment and carbon-star production in metal-rich populations. *Mon. Not. R. Astron. Soc.* **445**, 347–358 (2014).
24. Karakas, A. I. Updated stellar yields from asymptotic giant branch models. *Mon. Not. R. Astron. Soc.* **403**, 1413–1425 (2010).
25. Vassiliadis, E. & Wood, P. R. Evolution of low- and intermediate-mass stars to the end of the asymptotic giant branch with mass loss. *Astrophys. J.* **413**, 641–657 (1993).
26. Marigo, P. & Aringer, B. Low-temperature gas opacity. *ÆSOPUS*: a versatile and quick computational tool. *Astron. Astrophys.* **508**, 1539–1569 (2009).
27. Lattanzio, J. C. The asymptotic giant branch evolution of 1.0-3.0 solar mass stars as a function of mass and composition. *Astrophys. J.* **311**, 708–730 (1986).
28. Longland, R., Iliadis, C. & Karakas, A. I. Reaction rates for the s-process neutron source $^{22}\text{Ne} + \alpha$. *Phys. Rev. C* **85**, 065809 (2012).

Acknowledgements We thank Onno Pols and Rob Izzard for useful insights on binary systems and Paola Marigo for discussion of our results. M. L. is a Momentum (“Lendület-2014” Programme) project leader of the Hungarian Academy of Sciences. M. L. and A. I. K. are grateful for the support of the NCI National Facility at the ANU.

Author contributions M. L. designed and carried out the research, run the nucleosynthesis models, prepared the figures, and wrote the paper. A. I. K. run the stellar structure models, discussed

the results, and wrote the paper. C. G. B. played a key role in the set up and running of the underground experiment of the $^{17}\text{O}(\text{p},\alpha)^{14}\text{N}$ reaction and analysed the data to derive the new rate. M. A. contributed to run the experiment and wrote the paper. L. R. N. contributed to the collection of the stardust grain data, discussed the results, prepared the figures, and wrote the paper. The other authors are co-investigators who set up and ran the underground experiment that lasted about three years, from 2012 to 2015, and made the measurements possible. O. S. also discussed the results.

Author information Correspondence and requests for materials should be addressed to M. Lugaro (email: maria.lugaro@csfk.mta.hu).

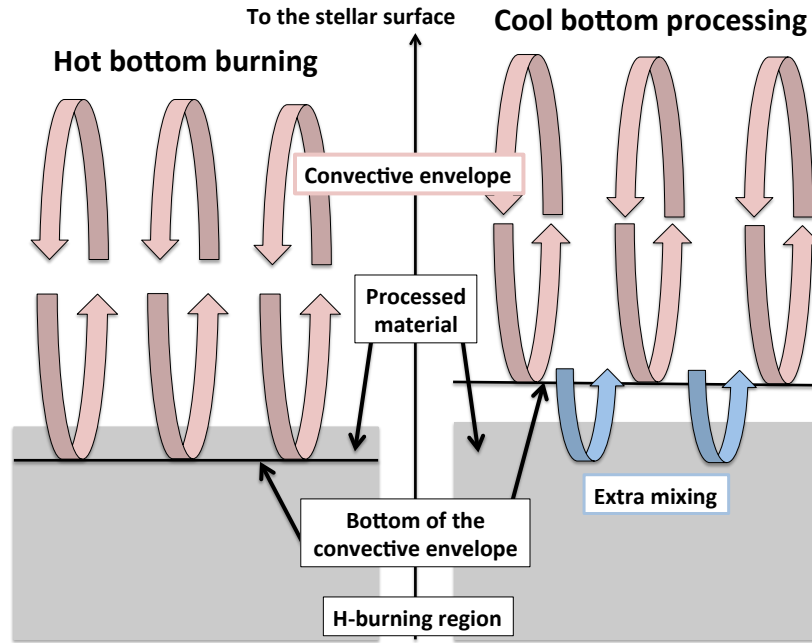


Figure 1: Schematic diagram of the internal structure of AGB stars at the interface between the H-burning region and the convective envelope. Hot bottom burning (HBB, left) and cool bottom processing (CBP, right) take place in massive and low-mass AGB stars, respectively, and carry material processed in the H-burning region to stellar surface. The main differences between the two cases are that: (1) material is processed at higher temperatures but lower densities in the case of HBB, with respect to CBP; and (2) mixing occurs via convection in the case of HBB, while non-convective extra mixing needs to be invoked in the case of CBP.

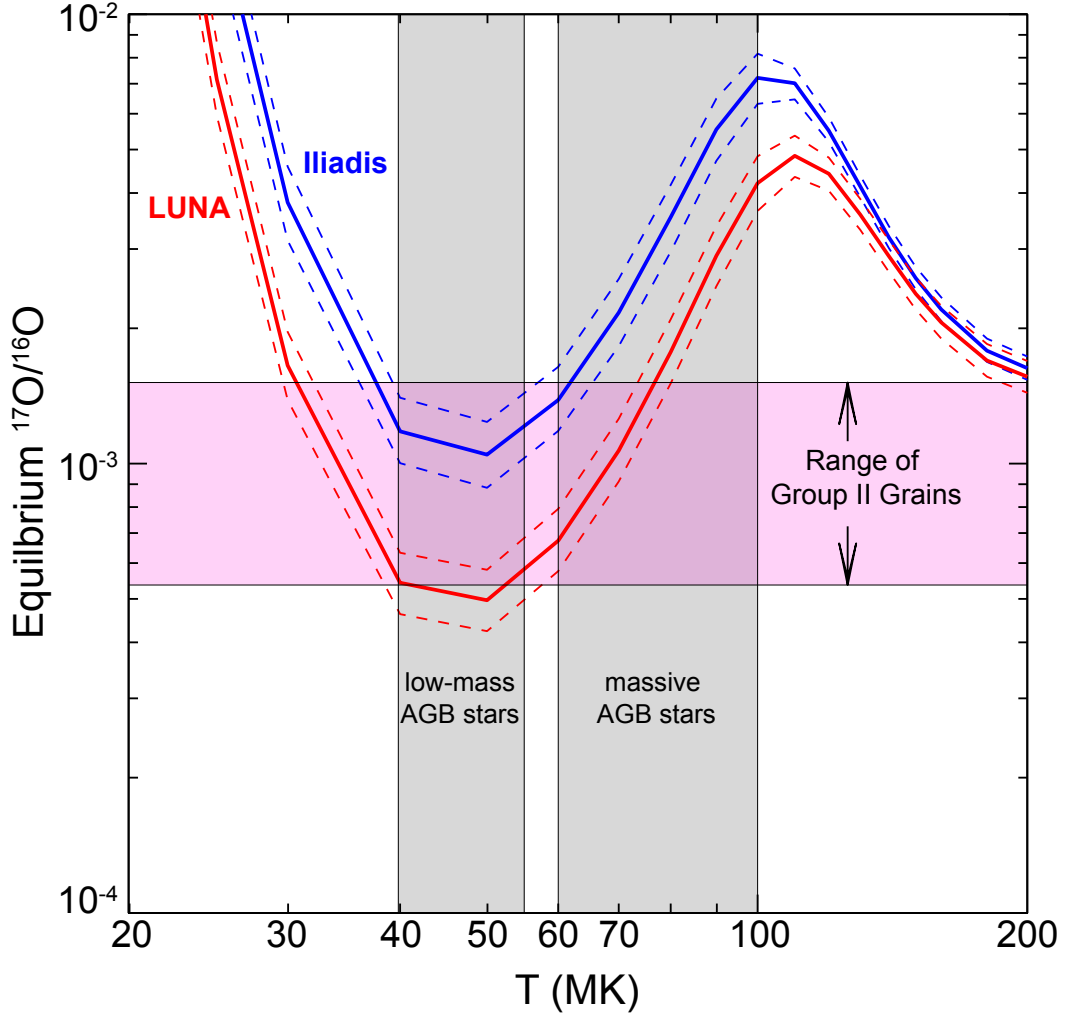


Figure 2: Equilibrium $^{17}\text{O}/^{16}\text{O}$ ratio defined as the ratio of the production to destruction rates of ^{17}O in the temperature range of interest for AGB stars. We used the recommended (thick solid lines) and the lower and upper limits (thin dashed lines, essentially corresponding to the 1σ experimental uncertainty of the strength of the 64.5 keV resonance) of the $^{17}\text{O}(\text{p},\alpha)^{14}\text{N}$ reaction rate from LUNA⁶ and Iliadis *et al.*¹². The horizontal pink band shows the range of $^{17}\text{O}/^{16}\text{O}$ values observed in Group II grains. The typical temperature ranges for CBP in low-mass AGB stars and for HBB in massive AGB stars are shown as grey vertical bands.

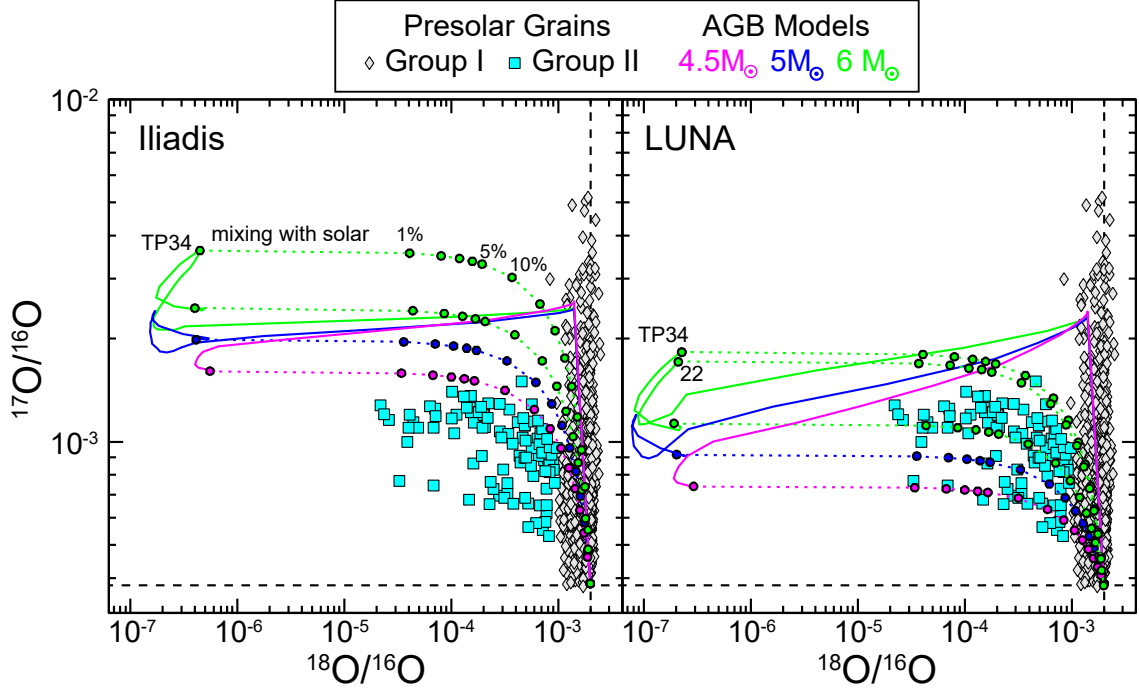


Figure 3: Evolution of the oxygen isotopic ratios at the surface of AGB models of different masses. The evolutionary (solid) lines in panel a were calculated using the old (Iliadis¹²) and in panel b using the new (LUNA⁶) $^{17}\text{O}(p,\alpha)^{14}\text{N}$ reaction rate. Uncertainties in either rate translate into changes in the $^{17}\text{O}/^{16}\text{O}$ ratio by at most 20%, i.e., within the differences between the different stellar models. Isotopic ratios observed in Group II grains (filled square symbols²¹ with error bars typically within the size of the symbol) cannot be reproduced by the old rate, regardless of the amount of dilution of AGB material with solar material (dotted lines), but are well reproduced with the new rate. The dilution is applied to the AGB composition at the end of the evolution for the three masses and, as examples, also at one-half and one-third of the AGB lifetime for the 6 M_{\odot} star (labels TP34 and 22 indicate that the star evolved, respectively, through 34 and 22 thermal instabilities of the He shell out of the 53 computed in the models). Dashed vertical and horizontal lines indicate solar ratios for reference.

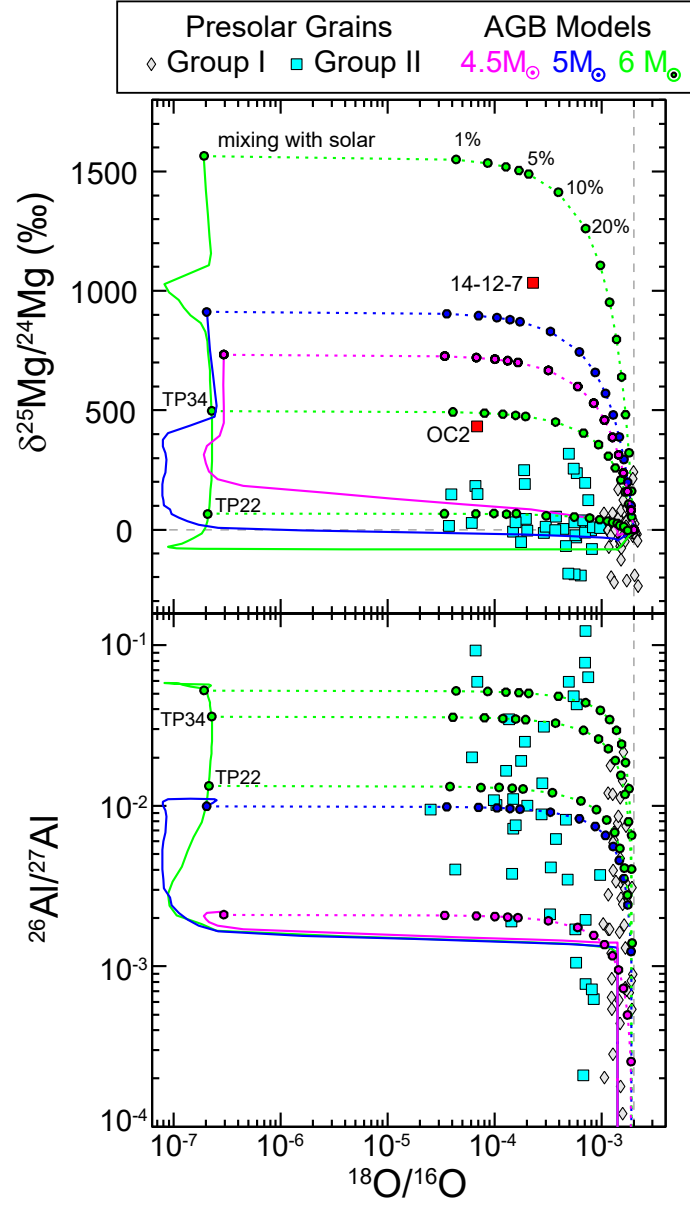


Figure 4: Evolution of selected Mg versus O (a) and Al versus O (b) isotopic ratios at the surface of AGB models of different masses. Same as Figure 3, with models calculated with the LUNA rate. $\delta^{25}\text{Mg}/^{24}\text{Mg}$ -values represent permil variations with respect to the solar system value. The two spinel grains with excesses in ^{25}Mg (OC2 and 14-12-7) are highlighted in red.

Methods

Stellar models

Stellar structure models with metallicities (Z) from half to double solar (where solar is 0.014²²) were selected from the large set presented by Karakas²³ computed with the Monash-Stromlo code²⁴. No mass-loss was assumed on the red giant branch and the Vassiliadis & Wood²⁵ mass-loss formulation was used on the AGB. The C-rich and N-rich low-temperature opacity tables were taken from Marigo & Aringer²⁶. Convection was approximated using the mixing length theory with a mixing-length parameter of 1.86 in all calculations. No convective overshoot was applied, although the algorithm described by Lattanzio²⁷ was used to search for a neutrally stable point for the border between convective and radiative zones.

From the models presented by Karakas²³, in the Supplementary Table 1 we present a selection with initial masses from 4.5 to 8 M_{\odot} with canonical values of the He content. More details on the physical quantities of the models can be found in Table 1 of Karakas²³. In Supplementary Table 1 we only report a summary of those that are most relevant here: the total number of thermal instabilities of the He-burning shell (thermal pulses, TPs); the maximum temperature at the base of the convective envelope ($T_{\text{bce}}^{\text{max}}$); the maximum temperature achieved in the inter-shell ($T_{\text{inter-shell}}^{\text{max}}$); and the mass lost during the whole evolution ($M_{\text{lost}}^{\text{total}}$). All the models experienced $T_{\text{bce}}^{\text{max}}$ high enough to activate HBB, except for the 5 M_{\odot} model of $Z = 0.03$. It should be noted that the mass and metallicity ranges at which HBB occurs are model dependent: for the same mass and metallicity, models using more or less efficient convection, for example, via a different mixing

length parameter or different mixing schemes, result in different temperatures^{7,8}. All our stellar models also experienced efficient third dredge-up, i.e., C-rich material being carried from the He-rich inter-shell to the convective envelope. This is also model dependent. Overshooting at the base of the convective region associated with the TPs is not included in our models. In combination with the third dredge-up it would enrich the envelope in ^{16}O . However, this would not change the oxygen isotopic ratios at the stellar surface since HBB efficiently brings them to their equilibrium values, similarly to the case of the carbon isotopic ratios. In the lower-mass stars where HBB is not activated, efficient third dredge-up of ^{16}O would be accompanied by efficient third dredge-up of ^{12}C , producing a C-rich envelope where the oxide and silicate grains considered here do not form.

Because of both the large dilution and the effect of HBB, most of the models lead to O-rich surfaces – the condition for the formation of oxide and silicate grains of interest here – during their whole evolution, except for the $4.5 M_{\odot}$ model of $Z=0.014$ and the $5 M_{\odot}$ model of $Z=0.007$. These latter become C-rich after the second last TP and the last TP, respectively, which results in 40–50% of the material ejected to be C-rich. For all the models, a relatively large fraction of the envelope material (20–30%) is still present when our calculations stopped converging. The abundances we calculated for the last model are either lower limits or a good approximation to the final enrichment, depending on possible further occurrence of third dredge-ups episodes beyond the point where our models stop converging.

We fed the computed stellar structure into the Monash post-processing code to calculate the detailed nucleosynthesis by solving simultaneously the abundance changes wrought by nuclear reactions and by convection using a “donor cell” advective scheme with two-streams (up and

down) mixing. The simultaneous treatment of mixing and burning is required to model HBB in detail because nuclear reactions occur that may have timescales similar or shorter than the mixing timescales, also as function of the location in the envelope. In these cases it is not possible to make the assumption of instantaneous mixing at an average burning rate. Essentially our method couples mixing and burning together in the post processing to obtain the nucleosynthesis, while the energetic feedback of HBB is taken from the structure calculations performed using instantaneous mixing. The nucleosynthesis of elements up to Pb and Bi from the complete set of the models of Karakas²³ with He canonical abundance can be found in Karakas & Lugaro⁹, together with a full discussion of the results. Briefly, in models that experience HBB, $T_{\text{bce}}^{\text{max}}$ is the main feature controlling the composition of the stellar surface, and specifically the oxygen and aluminium ratios that are measured in oxide and silicate stardust grains. In massive AGB stars of metallicity around solar the Mg composition is affected mainly by the activation of the $^{22}\text{Ne}(\alpha, n)^{25}\text{Mg}$ and $^{22}\text{Ne}(\alpha, \gamma)^{26}\text{Mg}$ reactions in the He-rich inter-shell – where $T_{\text{inter-shell}}^{\text{max}}$ is well above the activation temperature ($T \approx 300$ MK) of these reactions in all the models – and the subsequent third dredge-up of this material to the stellar surface. With respect to Karakas & Lugaro⁹, we updated the $^{22}\text{Ne} + \alpha$ reaction rates from Iliadis *et al.*¹² to Longland *et al.*²⁸ and the $^{25}\text{Mg} + \gamma$ reaction rates from Iliadis *et al.*¹² to Straniero *et al.*²⁰. Also, in the present study, we limited our calculations to a small network of 77 nuclear species, from neutrons to sulfur, plus the elements around the Fe peak, as described, e.g., in Karakas²⁴. This choice allowed us to run each model in a few hours and test different values of the $^{17}\text{O}(\text{p}, \alpha)^{14}\text{N}$ reaction rate: the recommended, the upper limit, and the lower limit from both Iliadis *et al.*¹² and LUNA⁶. For the $^{16}\text{O}(\text{p}, \gamma)^{17}\text{F}$ rate we used the value recommended by Iliadis

*et al.*¹², which has an uncertainty of 7%⁵. For the initial composition, we used Asplund *et al.*²² for the solar metallicity models, scaled down or up by factor of two for the $Z=0.007$ and $Z=0.03$ models, respectively. While we calculated detailed model predictions for all the models listed in the Supplementary Table 1, in the figures and discussion we focus on the 4.5, 5, and 6 M_{\odot} models with $Z=0.014$ only, for sake of clarity. Models with different metallicities in the same mass range have similar $T_{\text{bce}}^{\text{max}}$ and provide similar results, except for the 5 M_{\odot} model of $Z=0.03$, which does not experience HBB but remains O-rich due to the low efficiency of the third dredge-up combined with the high initial O abundance. On the other hand, the 8 M_{\odot} models have too high $T_{\text{bce}}^{\text{max}}$ to provide a match with the grain data (see Figure 2). Stellar population synthesis models are needed to assess whether a number of Group I grains may also have originated from super-solar metallicity O-rich massive AGB stars that do not experience HBB.

Table 1: Summary of the physical properties of a selection of AGB models with initial masses (M, Column 1) from 4.5 to 8 M_{\odot} and metallicities (Z, Column 2) half-solar (0.007), solar (0.014), and twice-solar (0.03). Column 3: the total number of thermal pulses (TPs) of the He-burning shell; Column 4: the maximum temperature at the base of the convective envelope; Column 5: the maximum temperature in the inter-shell; Column 6: the mass lost during the whole evolution.

M (M_{\odot})	Z	No. of TP	$T_{\text{bce}}^{\text{max}}$ (MK)	$T_{\text{inter-shell}}^{\text{max}}$ (MK)	$M_{\text{lost}}^{\text{total}}$ (M_{\odot})
5	0.007	59	82.9	357	4.11
4.5	0.014	31	63.5	356	3.64
5	0.014	41	75.4	354	4.12
6	0.014	53	85.5	365	5.08
8	0.014	67	100	376	6.94
5	0.03	26	54.2	345	4.13
5.5	0.03	31	64.7	348	4.62
6	0.03	33	71.2	352	5.09
8	0.03	63	94.0	373	6.95